nuclear fusion
IAEA

PAPER • OPEN ACCESS

Overview of material migration and erosion experiments in the full-tungsten WEST tokamak during Phase 1 and Phase 2 operations

To cite this article: A. Hakola *et al* 2026 *Nucl. Fusion* **66** 086041

View the article online for updates and enhancements.

You may also like

- Transport in high-performance plasmas of the TJ-II stellarator: from first-principles simulations to experimental validation
J.M. García-Regaña, D. Alegre, J.A. Alonso et al.
- Inward particle flux caused by low-frequency electric fluctuations in the edge region of dipole magnetic field configuration
H. Saitoh, H. Mimura, S. Aoyagi et al.
- Towards digital twins of fusion systems
F. Jenko, J. Ball, D. Borodin et al.

This content was downloaded from IP address 78.1.121.7 on 24/11/2026 at 10:25

OPEN ACCESS
IOP Publishing | International Atomic Energy Agency Nuclear Fusion
Nucl. Fusion **66** (2026) 086041 (16pp) https://doi.org/10.1088/1741-4326/ae855e

Overview of material migration and erosion experiments in the full-tungsten WEST tokamak during Phase 1 and Phase 2 operations

A. Hakola[1,*], M. Diez[2], N. Fedorczak[2], J. Gaspar[3], E. Tsitrone[2], M. Balden[4], Y. Corre[2], S. Di Genova[2], A. Huart[2], C. Martin[5], I. Bogdanovic Radovic[6], E. Fortuna-Zalesna[7], E. Grigore[8], I. Jõgi[9], M. Kelemen[10], K. Krieger[4], A. Lagoyannis[11], J. Likonen[1], S. Markelj[10], R. Mateus[12], K. Mergia[11], P. Paris[9], P. Petersson[13], Z. Siketic[6], P. Tsavalas[11], T. Vuoriheimo[14], A. Widdowson[15], the WEST Team[a] and the EUROfusion Tokamak Exploitation Team[b]

[1] VTT Technical Research Centre of Finland Ltd, Espoo, Finland
[2] CEA, IRFM, Saint-Paul-lez-Durance, France
[3] Aix-Marseille University, CNRS, IUSTI, Marseille, France
[4] Max-Planck-Institut für Plasmaphysik, Garching, Germany
[5] Aix-Marseille University, CNRS, PIIM, Marseille, France
[6] Ruđer Bošković Institute, Zagreb, Croatia
[7] Warsaw University of Technology, Warsaw, Poland
[8] National Institute for Laser, Plasma and Radiation Physics, Bucharest, Romania
[9] University of Tartu, Tartu, Estonia
[10] Jožef Stefan Institute, Ljubljana, Slovenia
[11] National Centre for Scientific Research 'Demokritos', Athens, Greece
[12] IPFN, Instituto Superior Técnico, Universidade de Lisboa, Bobadela, Portugal
[13] KTH Royal Institute of Technology, Stockholm, Sweden
[14] University of Helsinki, Helsinki, Finland
[15] UKAEA, Culham Science Centre, Abingdon, United Kingdom of Great Britain and Northern Ireland

E-mail: antti.hakola@vtt.fi

Received 16 March 2026, revised 29 June 2026
Accepted for publication 2 July 2026
Published 16 July 2026

Abstract

This paper gives an overview of erosion and migration studies of tungsten (W) in the WEST tokamak during its Phase 1 (2016–2021) and Phase 2 (from 2022) experimental campaigns with a focus on plasma-facing components (PFCs) at the divertor. In Phase 1, gross erosion of PFCs is in line with observations from other major fusion devices and attributed to low-Z impurities in

[a] See http://west.cea.fr/WESTteam for the WEST Team.
[b] See Vianello *et al* 2026 (https://doi.org/10.1088/1741-4326/ae71ec) for the EUROfusion Tokamak Exploitation Team.
[*] Author to whom any correspondence should be addressed.

Original content from this work may be used under the terms of the Creative Commons Attribution 4.0 licence. Any further distribution of this work must maintain attribution to the author(s) and the title of the work, journal citation and DOI.

the plasma. In addition, a strong asymmetry is observed between the high- (inner) and low-field (outer) side divertor targets, in favour of the inner side. Net erosion at rates of <0.5 nm s^{-1} is measured around the strike points while the remaining areas are dominated by net deposition. The thickest deposited layers (up to 50 μm) with the most complex structures result from a cumulated plasma exposure of $\sim$7 h. The overall erosion-deposition pattern is further influenced by the strong magnetic ripple of WEST, which can result in almost an order of magnitude difference between the maxima and minima of the ripple. In Phase 2, increasing plasma fluence leads to the deposits growing to hundreds of micrometres in thickness. At the same time, erosion proceeds at a constant rate and can reach values up to 30 μm in $\sim$18 h of plasma time. In the main chamber, erosion is weaker than at the divertor but especially at low densities it can result in notable transport of W into the core. In addition, upon switching on the ICRF antennas, W sputtering on the close-by limiter structures can increase by a factor of more than 10. Modelling is able to catch many of the observed phenomena in Phase 1, with the exception of the inner–outer asymmetry and the formation of the thick deposits. In contrast, the patterns during the high-fluence operations in Phase 2 require more work to be reproduced.

Keywords: erosion, WEST, tungsten, deposited layer, fluence

(Some figures may appear in colour only in the online journal)

1. Introduction

Tungsten (W) is the primary candidate material for plasma-facing components (PFCs) in future fusion reactors [1]. Tungsten has several advantages over traditionally used low-Z materials such as carbon (C) or beryllium (Be): a high melting point, large thermal conductivity, and small erosion yield by impinging plasma particles, in addition to which tungsten shows low activation by neutrons and limited retention of plasma fuel during reactor operations. However, as a heavy element ($Z = 74$), tungsten particles in the core plasma can lead to considerable radiation losses even at minute concentrations (<0.01 at.%). Operation of fusion devices in the presence of W-based PFCs is therefore under active investigations including obtaining a concise picture of the relevant plasma–wall interaction (PWI) phenomena as well as the evolution of PFCs upon cumulating exposure to high plasma fluences. In recent years, such studies have extensively been carried out in several tokamaks with full or partial W coverage, including ASDEX Upgrade (AUG) [2], JET [3], EAST [4], and WEST [5–8]. In WEST and EAST, superconducting coils offer the possibility of running long plasma discharges and testing several PFC solutions in an ITER-relevant environment [9]. In contrast, AUG provides the possibility to operate at high power-to-radius ratios ($P_{\rm sep}/R$), mimicking the heat-flux conditions expected in next-generation fusion pilot plants.

We investigate here the erosion and deposition behaviour of W during extended plasma exposure in WEST with the focus at the *divertor* region. In this context, one should distinguish between *gross erosion*, i.e. primary sputtering of W from the PFCs, and *net erosion* which takes (prompt) re-deposition of W onto the components into account [2]. Besides becoming re-deposited on the surface, the sputtered W atoms can migrate in the scrape-off layer (SOL) plasma into other regions and form co-deposited layers together with fuel and impurity particles. The structure, composition, and thermo-mechanical properties of the deposits will depend on several parameters including the selected operational scenario and characteristics of the PFC surface. In future devices, the layers may contain significant amounts of plasma fuel—hydrogen (H), deuterium (D), and tritium (T)—which calls for detailed investigations during and after a pre-determined series of discharges, in particular to correctly estimate the radioactive tritium inventory for the safety case of a fusion reactor.

The ultimate goal of this work is to obtain insights on the balance between gross and net erosion throughout experimental campaigns on WEST and to provide input data to be used in predictive simulations for future campaigns and devices. The new ITER baseline [10] has further increased the interest in clarifying erosion and re-deposition patterns of W-based PFCs everywhere in the reactor vessel. Contrary to earlier designs, both the divertor and the main chamber regions of ITER will consist of PFCs exclusively made of W.

Data collected from previous experiments on AUG and JET show that large net erosion occurs predominantly close to the outer (low-field side (LFS)) strike point (OSP), while net deposition typically dominates at the inner (high-field side (HFS)) strike-point (ISP) region. In the main chamber, net erosion and deposition are even more local phenomena, and the determined erosion and deposition rates can be highly sensitive to changes in the SOL plasma parameters. Existing knowledge is collected in [11] and summarized below:

- The largest W gross erosion typically occurs in H-mode during the edge-localised mode (ELM) bursts (*intra-ELM phase*) and is governed by the incoming plasma particles. In between the ELMs (*inter-ELM phase*) and in L-mode, impurity ions (intrinsic or seeded ones) are the dominant sputtering species.

- Besides physical sputtering by particle bombardment, erosion of W PFCs can also take place via the formation of tungsten hydride molecules in a process referred to as chemically assisted physical sputtering (CAPS). Erosion by CAPS is relevant only at low energies below the threshold for physical sputtering.
- In the inter-ELM conditions and in L-mode, W sputtering can be efficiently mitigated by operating in the (semi)*detached divertor* regime, which corresponds to low energies for the incoming particles in the divertor plasma. In the intra-ELM phase, the high energy for the particles makes full suppression of PFC erosion almost impossible.
- In the main-chamber regions, W gross erosion is generally 10 or 100 times lower than what has been measured at the divertor, excluding specific limiter structures at the LFS midplane.
- W eroded in the main chamber can more readily enter the core plasma due to less efficient screening of the impurities than is the situation at the divertor.
- Net erosion is also higher in H-mode than in L-mode; however, the increase is less pronounced than in the case of gross erosion, possibly due to enhanced re-deposition.
- Surface roughness can reduce W net erosion by an order of magnitude when comparing atomically smooth surfaces to technically rough ones (mean roughness values a few μm).

The results reported hereafter originate from analyses performed during and after several individual experimental campaigns on WEST, mainly in the L-mode regime. The conclusions drawn will be compared to the established material-migration picture in metallic fusion devices. In addition, results from interpretative modelling efforts will be reviewed. Section 2 introduces the WEST tokamak, the experimental campaigns carried out there (until spring 2025), description of wall components removed for subsequent analyses, and a description of techniques applied for their post-exposure characterization. The experimental results for W erosion, migration, and deposition are discussed in sections 3 (Phase 1) and 4 (Phase 2), the main difference being a largely increased exposure fluence during individual campaigns from Phase 1 to Phase 2 due to continued progress in extending the duration of individual plasma discharges. Section 5 reviews the modelling efforts made, and finally the entire work is concluded in section 6. This contribution will be an overview and synthesis of the obtained results while in-depth discussion of the underlying physics mechanisms is left for future publications. In addition, the details of individual experiments as well as the methodology of the applied analysis and simulation tools will be discussed in thematic articles that are referred to in the subsequent sections. These include assessments for the accuracy of the results and limitations in quantifying the total amount of erosion and deposition during the plasma operations on WEST.

2. Plasma operations on WEST and analyses performed on wall components

2.1. Overview of WEST and its experimental campaigns in different operational phases

WEST is a superconducting, medium-size tokamak (major radius $R_0 \sim 2.5$ m, minor radius $a_0 \sim 0.5$ m) which is capable of producing long plasma pulses (present record 22 min, see [12]) and enable investigating interactions between the PFCs and the plasma in a full-W environment [5, 6]. The operations can be carried out with toroidal magnetic fields up to $B_0 \sim 3.7$ T and using various radio frequency methods for auxiliary heating of the plasma. These include a Lower Hybrid Current Drive (LHCD) system consisting of two antennas (power levels 3–4 MW per antenna, frequency 3.7 GHz), an Ion Cyclotron Resonance Frequency (ICRF) setup whose antennas can couple 3–9 MW of heating power (frequency range 48–63 MHz), and finally a newly commissioned Electron Cyclotron Resonance Heating (ECRH) system operating at 105 GHz and designed to provide 1 MW of power during short pulses [9].

A specific feature of WEST is a strong modulation of the magnetic field in the toroidal direction, referred to as *magnetic ripple*, induced by the finite number of toroidal field coils with respect to the circumference of the torus. Overall, 18 maxima and minima of the field are observed on the divertor surfaces and such that each minimum (maximum) at the ISP region is accompanied with a maximum (minimum) around the OSP at the same toroidal location.

The operations on WEST have taken place in two distinct phases: Phase 1 from 2016 to 2021 and Phase 2 from 2022 onwards. Phase 1 has consisted of five experimental campaigns (C1–C5, plasma discharges from C2 onwards) whereas up to now 7 campaigns (C6–C11, until spring 2025) have taken place in Phase 2, so far in L-mode plasma operations. Glow-discharge boronizations have been regularly performed since the C3 campaign to condition the vessel walls. An overview of the different campaigns is summarized in table 1. In Phase 2 the main aim was to increase the particle fluence on the divertor target, which was greatly facilitated by longer durations for the individual discharges than is the case in Phase 1. Worth mentioning are also an extensive helium sub-campaign, performed during C4 (see [13]), and a deuterium high-fluence campaign in the end of C7 in hot ($T_e \sim 20$ eV) and attached divertor conditions [14]. In late 2025, another high-fluence operational phase was implemented under cold divertor conditions ($T_e < 5$ eV) but the results from this campaign phase are still pending and will be reported in future publications [15].

2.2. Wall components on WEST

WEST has an open (lower) divertor that consists of 12 sectors in the toroidal direction (labelled as Q1A, Q1B, Q2A,…, Q6B). Each sector is further composed of 38 plasma-facing units (PFUs) with a toroidal width in the range of 26–33 mm, from the inboard to the outboard side, and the poloidal length depending on the type of the PFU.

Table 1. Key parameters of the WEST experiments in Phase 1 (C2-C5) and Phase 2 (C6–C11, until spring 2025).

Campaign/Time	Plasma time	No. boronizations
C2/Nov17–Jan18	∼25 min	0
C3/Oct–Dec18	∼2 h	3
C4/Sep–Nov19	∼3 h 35 min	13
C5/Nov20–Jan21	∼1 h 15 min	2
C6 + C7/Dec22–Apr23	∼5 h 30 min	2
C8 + C9/Dec23–Apr24	∼5 h 45 min	5
C10 + C11/Dec24–Apr25	∼7 h	6

In Phase 1, a mix of passively-cooled, W-coated graphite PFUs and actively-cooled bulk W tiles, so-called ITER-grade PFUs was used. Each ITER-grade PFU consisted of 35 individual, 12-mm wide monoblocks (MBs), separated by 0.5 mm wide gaps and brazed on copper (Cu)-based cooling channels in the poloidal direction. For Phase 2, instead, a full actively-cooled divertor with the above-mentioned MB structure was installed as illustrated in figure 1. Excluding the ITER-grade PFUs during Phase 1 and a small region in the private flux region (PFR) without any shaping, all the components were installed in the divertor with a slight toroidal bevel (corresponding to a slope of 1°) similarly to what is foreseen for ITER, see figure 1; in the schematic view the bevel is largely exaggerated.

The W-coated PFUs were equipped with a 12 μm thick W layer on top of an intermediate Mo layer with a thickness of ∼3 μm. In addition, altogether eight *erosion-marker PFUs* were manufactured, by producing additional Mo (∼0.1 μm) and W (up to 2 μm) layers on top of the standard coated PFUs at selected poloidal and toroidal locations [7, 8, 16]. Schematic illustrations of the material combination on the coated PFUs can be found in figure 1.

The poloidal position at the divertor can be described by the so-called s coordinate which runs from the innermost divertor corner on the HFS to the outer edge of the PFU on the LFS. The coordinate system is illustrated for the different PFUs, both for the coated tiles and the MB structures in Phase 1 and Phase 2 in figure 2(*a*). Worth noting is that the W-coated PFUs consisted of two parts: the inner one at the HFS (poloidal length 326 mm) and the outer one at the LFS (poloidal length 256 mm).

During Phase 1, the ISP and OSP were predominantly located $s \sim$ 246–258 mm $s \sim$ 346–358 mm, respectively, corresponding to MB16 and MB24. However, the shapes of the strike-point profiles were quite different during the different campaigns as illustrated in figure 3(*a*); the figure shows the integrated strike-point time as a function of the s coordinate (and the MB number). Most notably, the ISP profile was the broadest with the main peak furthest into the SOL following C4 while the same campaign resulted in the most peaked profile around the OSP. In Phase 2, due to the high-fluence campaign performed in C7, prominent maxima were measured for the ISP (on MB16) and OSP (on MB25) as can be seen in figure 3(*b*).

In the main chamber, the PFC structures have varying specifications depending on into which regions they had been installed. During the C1–C4 campaigns, the inner-bumper and antenna-protection limiters consisted of W-coated carbon-fibre composite structures while boron nitride (BN) tiles were installed to replace the central parts of the limiters for the C5–C9 campaigns; starting from C10, the BN tiles were replaced with bulk-W ones. The baffle region as well as the upper divertor, for their part, are made of actively cooled CuCrZr structures with a W coating [5].

2.3. Gross and net erosion investigations on WEST

Gross erosion of W is primarily assessed via absolutely calibrated visible spectroscopy, focusing on the atomic line of neutral tungsten (WI) at 400.9 nm. The inverse photon efficiency conversion factor is S/XB ∼30 in attached divertor plasma conditions (around 20 eV) while it decreases to S/XB ∼20 once the electron temperature drops to 10 eV or below. The spectroscopy system can provide *in situ* information on the primary sputtering of PFUs during individual plasma discharges with a good coverage of the entire poloidal range at the divertor with a spatial resolution of better than 10 mm [17, 18].

Determining net erosion, instead, relies on post-exposure surface analyses of selected PFUs after their plasma exposure. During Phase 1, a number of W-coated PFUs, both standard and erosion markers, as well as ITER-like PFUs were removed separately after the C3, C4, and C5 campaigns and measured for their erosion and deposition patterns. Most of the erosion markers were mounted at the maxima of the magnetic ripple in sector Q2A except for two PFUs installed at the close-by minimum of the ripple in the same sector. Details can be found in figure 2(*b*). During the maintenance breaks in Phase 2, several actively-cooled MB structures became also available for detailed inspections.

For the post-exposure studies, a detailed analysis programme was compiled consisting of both full-tile measurements and more detailed investigations of small samples extracted from the coated PFCs or from individual MBs. The following methods have contributed to the formation of the database discussed here: (i) visual and microscopy investigations, including scanning electron microscopy (SEM), possibly assisted by focused ion beam (FIB) cuts, and transmission electron microscopy (TEM); (ii) compositional analyses utilizing various ion-beam techniques such as Rutherford backscattering spectrometry (RBS), nuclear reaction analysis (NRA), particle induced x-ray emission (PIXE), and time-of-flight elastic recoil detection analysis (TOF-ERDA) as well as energy dispersive x-ray spectroscopy (EDX) during SEM investigations; (iii) detailed elemental depth-profile studies by employing secondary ion mass spectrometry (SIMS), laser-induced breakdown spectroscopy (LIBS), and glow-discharge optical emission spectroscopy (GDOES); (iv) surface-sensitive methods, namely x-ray photoelectron spectroscopy (XPS) and Raman spectroscopy; and (v) thermal desorption spectroscopy (TDS) for obtaining the fuel inventory on the samples. Further details on the analyses and the results

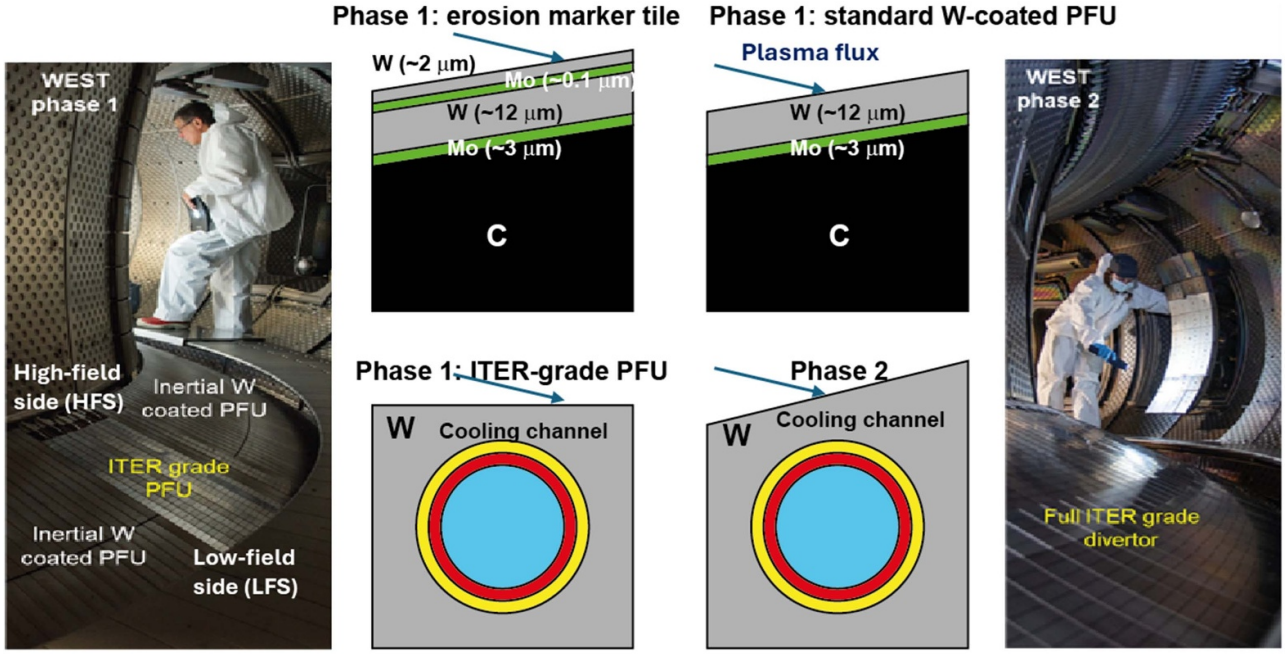


Figure 1. Photographs of the WEST divertor and main-chamber regions (left and right) together with schematic illustrations of the cross-sections of different PFUs in Phase 1 and Phase 2 including the direction of the plasma flux (blue arrows) and toroidal bevelling of the different PFU structures by 1°.

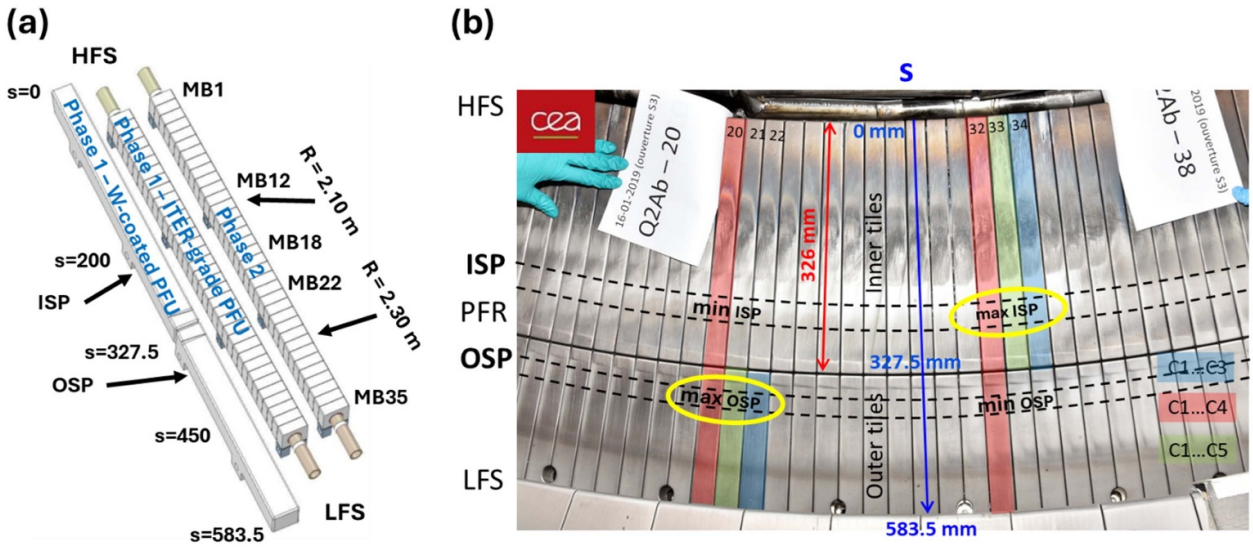


Figure 2. (*a*) Schematic layout of WEST PFUs together with reference values for the *s* coordinate, naming scheme for the MBs, as well as reference values for the major radius, *R*, at the divertor; (*b*) Photograph of the WEST divertor sector Q2A, highlighted with the locations of the marker tiles during the 2019 opening after C3. The maxima and minima of the toroidal ripple have been marked. Tiles marked in blue were removed after C3, those in red after C4, and the green ones after C5. Reproduced from [8]. © The Author(s). Published by IOP Publishing Ltd. CC BY 4.0. Each toroidal position (20–22 and 32–34 highlighted in the figure) contains two tiles: one at the HFS (from $s = 0$–326 mm), the other at the LFS (from $s = 327.5$–583.5 mm).

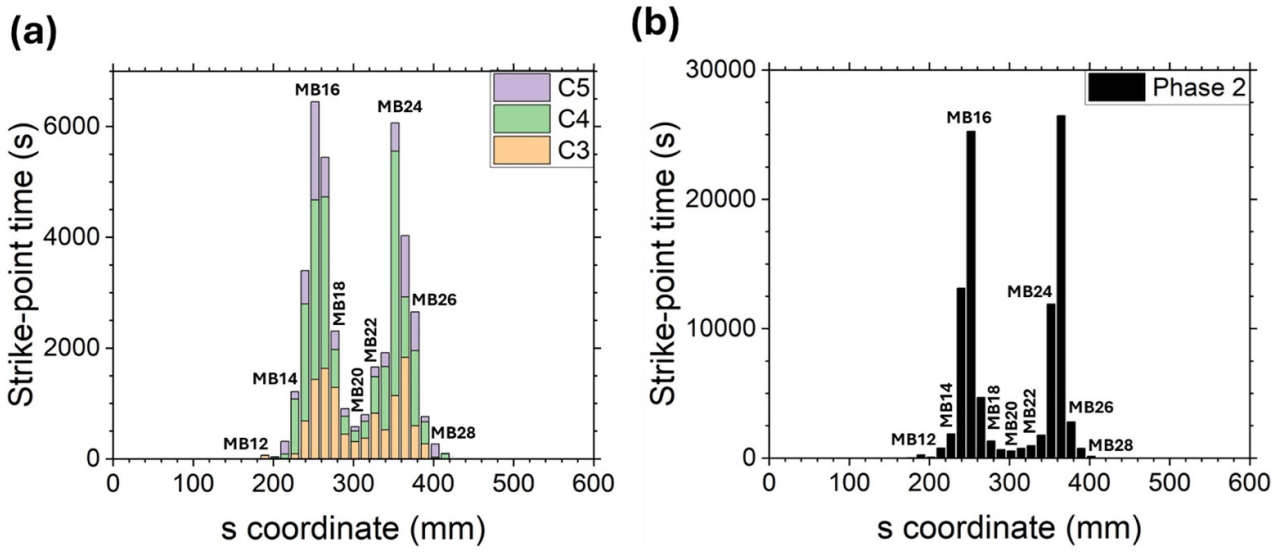


Figure 3. Strike-point time at the lower divertor of WEST as a function of the *s* coordinate (*a*) during Phase 1, separately for the C3, C4, and C5 campaigns and (*b*) during Phase 2 (until C11 campaign).

obtained are collected in [7, 8], and [19–26]. In addition, emissivity measurements were carried out to investigate net erosion of divertor PFCs, both *post mortem* and *in situ* [27].

All the methods will provide complementary information on the erosion and deposition patterns at different lateral and depth resolutions, analysis depths and analysis areas. Microscopy methods are the most local and can reveal even sub-μm features on the samples [8, 16, 19], while methods such as SIMS enable reconstructing detailed elemental depth profiles at depth resolutions down to a few nm [22].

3. Material migration during phase 1 operations on WEST

3.1. Gross erosion of W in the divertor and main-chamber regions

The determined gross-erosion rates of W during Phase 1 are in line with published data from other tokamaks with full or partial W coverage, peaking to 1–2 nm s^{-1} in L-mode plasmas [18, 28]. The strongest W erosion flux is observed at the divertor while in the main-chamber regions the erosion sources are substantially weaker, typically by one or two orders of magnitude as is the case in other machines with W PFCs [11]. However, when applying LHCD or ICRF heating, notable W emission can be observed from the limiter structures surrounding the respective antennas depending on the heating scheme and the power levels induced.

In a set of experiments where both ohmic and LHCD heating were used, W sputtering rates of 1–2 $\times$ 10^{20} s^{-1} m^{-2} at the divertor were determined with the electron temperature (T_e) spanning a broad range up to 50 eV; below 5 eV the W sources were almost non-existent [18]. Even higher values are possible if the ratio between the ion and electron temperatures upstream increases, resulting in hotter plasmas at the divertor targets [28].

Besides electron temperature, sputtering is largely governed by light impurities in the SOL plasma, whose overall concentration can reach values of 3 at.% or more in typical WEST L-mode plasma conditions [18]. Highly charged oxygen ions (O^{6+} and above) are identified to be strong contributors to W sputtering on the main-chamber antenna limiters. In contrast, O and C in their different ionization states are prominent sputtering agents at the divertor but they cannot solely explain the observed gross-erosion rates: boron (B) from glow-discharge boronizations and powder-dropper studies and nitrogen (N) from seeding experiments and plasma start-up procedures are needed to improve the match between experiments and modelling [29, 30]. Finally, self-sputtering by energetic W ions has been suggested to play a significant role in the sputtering of WEST divertor PFUs, on the basis of simulations in [31].

Another WEST-specific observation is a notable asymmetry in W sputtering between the ISP and OSP: in L-mode, sputtering can be a factor of 2–10 higher on the inner than on the outer strike-point area depending on the power entering the SOL as well as plasma density and gas [28] as can be seen in figure 4(*a*). Here, WI emission for different L-mode discharges at varying LHCD heating powers ($B_t = 3.6$ T, $I_p = 700$ kA, line-averaged density 4 $\times$ 10^{19} m^{-2}, radiated fraction ~50%) is plotted at different locations on the inner and outer divertor surfaces with respect to the major radius around the ripple maximum. The reason for the asymmetry is proposed to be associated with drift flows as will be discussed in section 5.1 and as has been earlier observed in other devices, e.g. at JET [32]. Comparison between D and He plasmas (figures 4(*a*) and (*b*), respectively) shows that gross erosion is more intense in He, by an order of magnitude, and pertains at higher densities than is the case for D plasmas. Moreover, the same inner–outer asymmetry but much more prominently than in the case of D is measured. In the He case, the data is extracted from ohmic plasma scenarios (same B_t

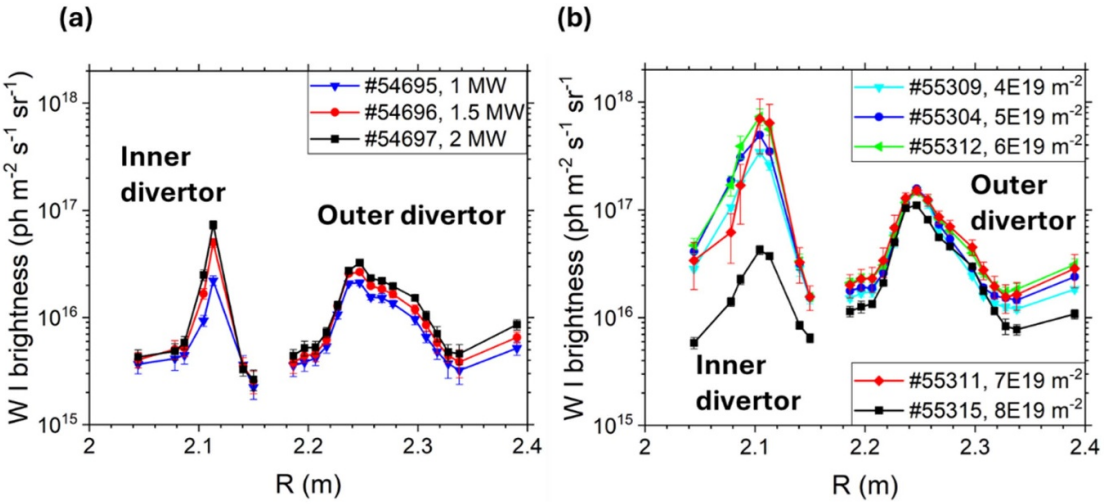


Figure 4. Divertor WI (400.9 nm) line emission extracted for different ohmic plasmas in (*a*) deuterium at varying LHCD heating powers as indicated in the legend and in (*b*) helium at different line-averaged densities as a function of the major radius R (correspondence between R and the divertor s coordinate can be found in figure 2 such that the ISP is located at $R \sim 2.10$ m and OSP at $R \sim 2.25$ m).

and I_p as for the D pulses, heating power ∼1 MW, radiated fraction ∼80%) and shows a slight dependence on the line-averaged density of the plasma, most pronounced in the densest plasmas.

3.2. Net erosion and deposition of W at the divertor

3.2.1. Toroidal and poloidal net erosion patterns. The data obtained from the erosion marker tiles indicate distinct net-erosion regions both at the ISP and OSP regions as illustrated in figure 5(*a*). Somewhat contrary to the data from other metallic devices, the erosion peaks are strong also on the inner side, almost comparable to the values extracted from the vicinity of the OSP. Worth noticing is that the absolute values for net erosion generally exceed the thickness of the topmost marker layers (>2 μm), inducing uncertainties in the determined erosion rates during an entire experimental campaign [16]. Results from RBS measurements were thus combined with the available GDOES, SIMS, and LIBS depth profiles and with local information extracted from specific FIB-prepared cross sections to estimate erosion characteristics of the relatively thick standard W coatings on selected PFUs. For some of these tiles, also detailed erosion determinations were performed by comparing the thickness of the remaining W coating to that of an unexposed reference PFU. This way, the limitations set by the marker layers could be circumvented, in particular after the C4 and C5 campaigns. Overall, the maximum net-erosion rates were estimated to 0.1–0.3 nm s^{-1}, in agreement with campaign-integrated data from AUG at the OSP [2]. The numbers were obtained by dividing the change in layer thickness by the overall plasma flat-top time during the corresponding sequence of operations, by assuming linear dependence between erosion and the exposure time. The total error bars lie in the range of 10%–15% (see, e.g. [33]).

More detailed erosion investigations were carried out for five pairs of actively-cooled inner and outer divertor PFUs, removed from different toroidal positions of a single sector (Q3A) after the C5 campaign. This way not only the poloidal but also toroidal dependence of net erosion within a single ripple period could be estimated [16]. The following conclusions can be drawn, as also illustrated in figure 5(*b*).

- In the toroidal direction, the erosion maxima and minima follow the pattern determined by the magnetic ripple and exhibit a factor of 2–10 difference between the maxima and minima.
- The absolute values of net erosion reach values down to 6–8 μm, which can be converted into an average net erosion rate of 0.3 nm s^{-1}.
- The main erosion peak does not occur toroidally at the centre of the tile but is shifted away from the leading edge due to shaping of the tiles. In addition, at the ISP region a secondary peak appears close to the leading edge, partly but not fully inside the magnetically shadowed area. The reason for such behaviour requires further investigations but is proposed to be related to ripple-induced fluctuations in the plasma flux.
- In the poloidal direction, the extent of the region dominated by net erosion is wider around the OSP (40 mm) than close to the ISP (20 mm). This could be partly explained by the electron-temperature and density profiles but also by the magnetic equilibrium that enables varying the X-point height from typically 40–110 mm leading to displacement of the ISP and OSP in the poloidal direction. Along with the ripple period, the erosion peak becomes poloidally shifted by 10–20 mm from a minimum to a maximum.
- The erosion peak is the strongest in the vicinity of the ISP (8 μm vs. 6 μm, ISP vs. OSP). The observations are qualitatively consistent with what figure 3 illustrates but the strong asymmetry in gross erosion by more than a factor of 2 in favour of the ISP is not visible in the net-erosion

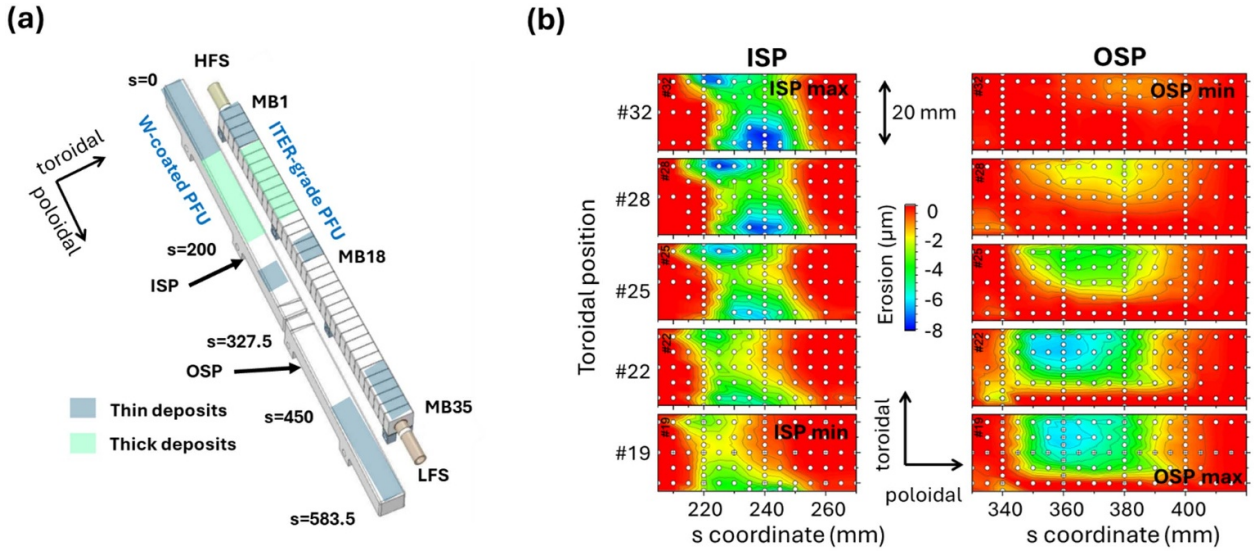


Figure 5. (*a*) Schematic illustration of the areas dominated by erosion (white) as well as thick and thin deposits (green and blue) during Phase 1 on W-coated and ITER-grade divertor PFUs; (*b*) Two-dimensional net erosion patterns measured for the series of W-coated standard tiles (from toroidal positions 19, 22, 25, 28, and 32, see figure 3) at the ISP and OSP regions. The toroidal extent of the analysis area is ∼25 mm, symmetrically on both sides of the central line, and the maxima/minima of the toroidal ripple in the ISP and OSP regions are marked in the patterns. The white dots mark the measuring positions which are inter- and extrapolated for the contour plot [16].

profiles. Here one should note that the peak in gross erosion at $R = 2.1$ m (see figure 4) corresponds to a value of $s = 200$ mm which is at the boundary between erosion- and deposition-dominated zones. A fraction of the W I signal may therefore originate from the proximity of the deposits. This is not the case on the OSP side, where the layers are generally thinner (see section 3.2.2).

From the data in figure 5(*b*) one can also obtain an estimate for the total amount of eroded tungsten during the entire Phase 1 (from C1 to C5). According to the analyses in [16], the eroded volume, toroidally and poloidally integrated over the divertor PFUs around the torus after 7.3 h of plasma, is ∼2 cm^3 and roughly equally distributed between the OSP and ISP regions. This is in line with the fact that even though the absolute gross erosion is higher at the ISP, the larger surface area around the OSP will lead to the comparable eroded volumes at the HFS and LFS divertor legs.

In the poloidal direction, the areas dominated by net erosion were altered from campaign to campaign, with the largest changes occurring between C3 and C4 and further from C4 to C5: after the C4 campaign, the erosion areas were strongly shifted poloidally towards the SOL and were also broader than during the rest of the Phase 1 operations [7, 8, 16]. The observations can be largely attributed to the different magnetic equilibria applied during the different campaigns as illustrated in figure 3(*a*): The distribution for the strike-point time quite different for the C3 and C4 campaigns throughout the divertor. Generally, the extent of the area dominated by net erosion is ∼40 mm close to the ISP while it is much wider on the outer side, around 60–100 mm with the lower limit corresponding to the C3 operations. A further consequence of this inherent evolution of the erosion patterns is that the integrated erosion at the OSP would increase up to 60% and thereby the ratio between the erosion volumes at the OSP and ISP could be up to a factor of two [16]. More detailed analyses are therefore required to reach the final conclusion on the magnitude of erosion in different parts of the divertor during Phase 1.

Concerning helium, it does not appear to have introduced notable nanoscale modifications such as W fuzz on the surface [2, 13] but may have contributed to the above-mentioned poloidal shifts of the erosion maxima. The absence of fuzz is most likely due to the limited time that the PFUs were exposed to sufficiently high surface temperatures (>700 °C), thus the accumulated fluence was marginal (∼2 × 10^{24} m^{-2}) to induce nanostructures on the PFU surfaces.

3.2.2. Structure and composition of deposited layers in phase 1. Notable deposited layers with thicknesses up to 50 μm have been measured on the erosion-marker and standard W-coated PFUs removed after the C3, C4, and C5 campaigns. Poloidally the layers are predominantly located in the inner divertor, with the thickest ones observed on the SOL side of the ISP as shown in figure 6(*a*), see [7, 8, 16, 19, 22, 25]. In addition, thinner layers have been measured throughout the peripheral SOL parts of the inner and outer PFUs as well as on the PFR side of the ISP. The characteristic poloidal extent of all these layers during Phase 1 operations on WEST can be found illustrated in figure 5(*a*).

The thickest layers show complex morphologies with a stratified structure and significant fractions of B, C, W, and O embedded. An example cross-sectional image of the layers is included as an inset in figure 6(*a*). Although the deposits exhibit strong local variations in appearance, structure, and composition laterally in the sub-mm or even in the μm-scale, on average the uppermost parts are more abundant in W while in deeper layers more B-rich features can be identified [19].

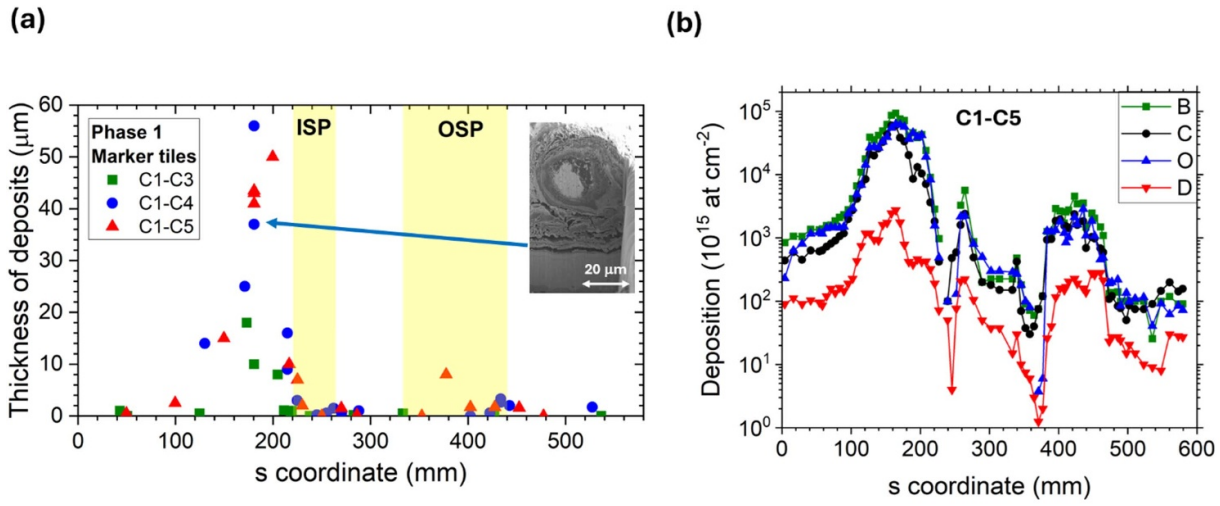


Figure 6. (*a*) Evolution of the thickness of deposited layers in Phase 1 together with an example cross-sectional SEM image of the structure of the thick co-deposited layers (here following exposures to C1–C4 campaigns) on WEST. The yellow regions denote the extent of typical ISP and OSP areas according to figure 5(*a*) [25]; (*b*) Poloidal NRA deposition profiles for B, C, O, and D during Phase 1, measured from marker tiles removed after the C5 campaign [16].

In addition, signs of arcing are visible on several locations leading to local damages and delamination of the deposits: around 25% of the layers or even the underlying coating can be affected [16]. Generally, the properties of the layers are comparable to those measured on AUG in its full-W operational phase even though the applied plasma scenarios are quite different between the two devices [34]: On AUG, several high-power H-mode discharges have been regularly carried out while the operations on WEST in Phase 1 have exclusively consisted of ohmic or L-mode plasmas at modest heating powers. The overall formation of the deposits appears therefore not to be that much dependent on the plasma parameters themselves but more on the delicate balance between material erosion, migration, and deposition on different poloidal regions at the divertor during the individual plasma discharges and full experimental campaigns on WEST. The latter clearly complicates associating the observations to a specific physics phenomenon.

The thin deposits on the PFUs have typically thicknesses of less than 0.5 μm and contain traces of various impurities almost independent of the exposure campaign. A notable exception are the somewhat thicker layers (1 μm or even beyond) which occur in narrow regions adjacent to the ISP in the PFR and in the transition zone from OSP towards the main SOL. On these layers, the very surface is typically dominated by B and O, followed by distinct sublayers where also metallic impurities such as chromium (Cr), iron (Fe), nickel (Ni), and copper are present together with elements from the coatings (Mo and W). Distinct sublayers (thicknesses in the range of some tens or hundreds of nm) can be observed on such deposits [19].

The deposited layers on the ITER-like PFUs are quite similar to the ones discussed above for the coated tiles except for the fact that they are 2–5 times thinner [16, 26]. This may be attributed to a smoother surface (mean arithmetic roughness $R_a \sim 1.2$ μm, for graphite $R_a \sim 2.5$ μm) of the MBs but also to their different toroidal positions with respect to the magnetic compared to the coated tiles: The analysed ITER-grade PFUs were roughly located in between a maximum and minimum while the marker tiles originated toroidally around the ripple maximum. Active cooling of the ITER-like PFUs may have also led to unfavourable conditions for deposits to be formed on the PFU surfaces due to their different surface temperature with respect to that on the coated tiles. Finally, particle and heat fluxes are lower on the ITER-grade PFUs (incident angle of the magnetic field line is typically 2.5° at the maximum ripple on flat surfaces) than on the W-coated graphite PFUs with the bevelled geometry (the corresponding magnetic-field angle is ∼3.5° at the maximum ripple) [35]. However, the impact angle would only result in a factor of 1.4 difference in deposition between the two PFU types, thus is not able to fully explain the observations.

Of the analysed light elements, boron is the most abundant while C and O are present roughly at similar concentrations and with surface densities some 1.5–2 smaller than those of B. This can be seen in figure 6(*b*), which shows measured surface densities for the different light elements (B, C, and O) as well as for D on the erosion-marker PFUs removed after the C5 campaign. Concerning fuel retention, the D profiles mainly follow those determined for the different low-Z elements proving that the main retention mechanism in Phase 1 is co-deposition. The D concentrations of the deposits are generally <5% and even in the thickest deposits never exceed ∼10%. Detailed XPS studies of the re-deposits imply the layers to consist of boron-carbide, tungsten-carbide, and tungsten-boride phases besides the formation of mixed B–C–O–D compounds and oxides [36]. Furthermore, boron nitrides as well as NH_3 and NH_2 structures could be identified due to

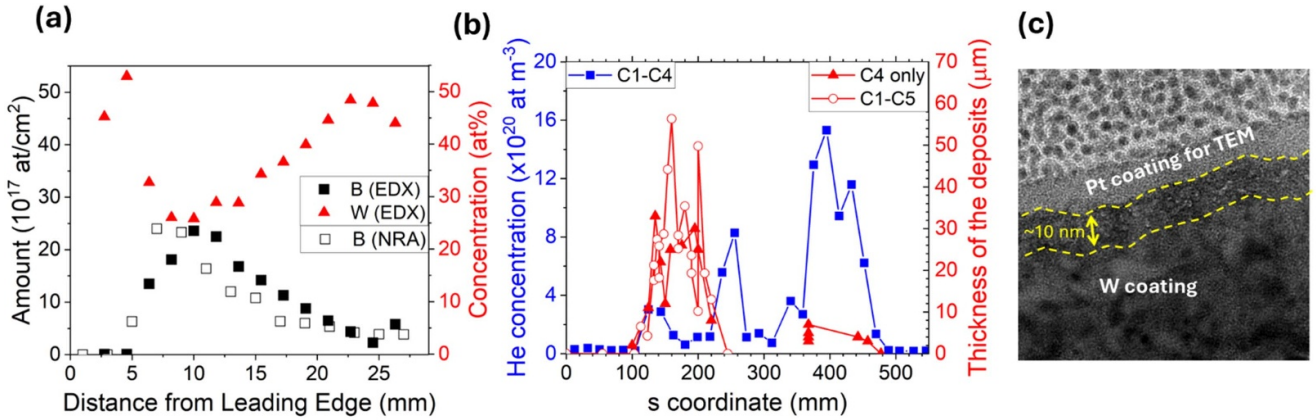


Figure 7. (*a*) B and W content on MB28 (Phase 1) along the toroidal direction [24]; (*b*) Helium content (blue) on standard W-coated PFUs (removed after C4) together with the thickness of deposited layers (red) on similar standard PFUs (data both after C4 and C5) [26]; (*c*) Example TEM image of the PFU surface around the maximum of He deposition ($s = 395$ mm) showing a thin region (10 nm) with He nanobubbles on the surface of the W coating. Reproduced from [26]. © 2026 The Authors. Published by Elsevier Ltd. CC BY 4.0.

the interaction between nitrogen impurities and the hydrogenic plasma compounds.

Analogously to the main net-erosion zones discussed in section 3.2.1, the areas dominated by deposition become wider or are poloidally shifted with accumulating plasma fluence. The thickest deposits during Phase 1 and the most notable changes in their structure and composition are measured after the C4 campaign where the plasma exposure was considerably longer compared to C3 and where the number of boronizations was larger. One should, nevertheless, keep in mind that the thickness and structure of the deposits are influenced by numerous successive cycles involving erosion, short- and long-range migration of material, deposition, and material influx from boronizations. As a result, when continuing the plasma exposure from C4 to the end of C5, in some poloidal regions the deposits continue to grow while on other regions comparable layers are measured after these two campaign phases. The short duration of the C5 campaign can also have impacted the balance.

Most deposition studies have been performed at a fixed toroidal position, along the central line of the PFCs. More recently additional data has become available also from measurements carried out along the toroidal direction from individual MBs. As an example, shown in figure 6(*a*), results from MB28, located somewhat off from the OSP on the SOL side and removed from WEST after the C4 campaign (sector Q3B, toroidal position #13 in between the ripple maximum and minimum) are discussed below [24]. The MB is dominated by net erosion, however, the analyses indicate locally several characteristic regions of deposits with varying morphologies, elemental compositions, and thicknesses. The leading edge of the MB contains thin deposits with B and N together with the typical metallic impurities and fuel (D and He). A correlation can be observed between the lateral profiles for the fuel and impurity elements and such that the D/B ratio remains approximately constant. This provides additional evidence that even around the OSP, co-deposition has a considerable impact on fuel retention. The thickness of the deposits increases sharply within a few mm from the leading edge until at ∼10 mm—corresponding to one third of the MB extent in the downstream direction—they gradually become thinner until mainly W from the substrate (together with oxygen and remnants of various light impurities) remains as illustrated in figure 7(*a*) close to 25 mm toroidally. Besides alterations in the thickness and composition of the deposits on the MB, also the surface morphology exhibits considerable heterogeneities at the sub-mm length scale including nanostructures, cracks, depressions, and grooves and such that deposition and fuel retention patterns are preferentially concentrated in the most prominent surface features. The observations give further proof for the local nature of erosion and deposition on technically rough PFCs of WEST. Worth noting is that similar abrupt changes in the characteristics of deposits is also observed in the poloidal direction when moving from the region of thick deposits towards the ISP [24].

The effect of toroidal ripple on the deposition patterns has not been studied in detail and remains an unresolved issue. Visual inspection suggests the thickest layers to be formed around a ripple maximum while microscopy analyses of specific areas on the thick deposits where arcing has led to partial delamination do not show any notable differences in layer thickness between different toroidal positions—implying deposition to be toroidally independent [16]. In contrast, data extracted from PFUs removed for analyses after Phase 2 quite clearly show deposits being much thicker around a ripple maximum than at the corresponding minimum as will be discussed in section 4.2.

Following the He operations [13] in the end of C4, analyses of the deposits demonstrate noticeable He inventories (corresponding to 5–10 at.%) close to the inner and outer strike points to the total measurable depth of about 1400×10^{15} at cm^{-2} (corresponding to 220 nm of pure W). This behaviour is depicted in figure 7(*b*). No differences were observed between the W-coated tiles and the ITER-grade MB surfaces and the 10-at.% maximum is in line with what could

be estimated from the overall He fluence on the strike-point regions during the He campaign (up to 5×10^{24} m^{-2}) [26]. The observations suggest that helium would be mainly retained via implantation in the high-flux areas. On the other hand, co-deposition is not completely excluded as shown by a second hump for the He surface density on the peripheral part of the region with thick deposits. Deposition deeper inside the layers cannot be excluded since the TOF-ERDA method used for the analyses is restricted to the vicinity of the PFC surface. Data from various MBs on one actively-cooled PFC give some indications that high He concentrations would occur close to the leading-edge part of the MB but depending on the poloidal position the peak may also be shifted towards the trailing edge. Despite the conditions being presumably favourable for triggering the growth of W fuzz, only some precursors for the characteristic nanoscale features could be observed [26] as illustrated in figure 7(*c*): an ∼10 nm thick layer of nanobubbles underneath the very surface is visible. Possible reason is that the surface temperatures were not high enough (>700 °C) during the plasma discharges to shift the balance from erosion and deposition to the formation and growth of nanoscale features.

The deposited layers can result in the production of dust in the vessel. During Phase 1, extensive investigations were carried out by collecting dust samples after the C4 and C5 campaigns and determining their size and weight distributions as well as composition and typical features of individual particles [36]. The most important observation is the presence of two distinct classes for the dust particles: one expectedly consisting of varying μm-scale particles (from a few to several tens of μm), the other one dominated by distinct nanoparticles. The micron-sized particles could have resulted from delamination of coated PFUs as well as from various droplets originating from off-normal events. The hypotheses are supported by the fact that the particles exhibited all kinds of shapes from spherical to highly irregular ones. Nanocavities were present on several of the particles after C4, most likely as a result of the He campaign. The nanodust, for its part, was discovered adhered on the μm-sized dust particles and proposed to be originated from condensation of supersaturated vapour in the vicinity of the big particles or from collisions between the ions and neutrals in the background plasma at low electron temperatures before solidification takes over [37].

4. Impact of pulse duration and fluence on material migration in phase 2

4.1. Gross and net erosion patterns

In Phase 2, the experimental activities focused on assessing erosion and migration of W during long-pulse operations and/or at high particle fluences. At the divertor, the same characteristic regions as after Phase 1 operations emerged: net erosion at the ISP and OSP regions, thick deposits on the SOL side of the inner strike point, and thin layers on the remaining areas (see figure 8(*a*)). In addition, a new class of *foil-like layers* could be identified around the edge parts of HFS or LFS MBs after C7 as also illustrated in figure 8(*a*). These deposits consist largely of W and are loosely adhered on magnetically shadowed areas, showing tendency to flake upon exposure to atmospheric conditions. Importantly, they are only seen to emerge following the high-fluence campaign: the deposits investigated after the C9 and C11 openings (see table i) were comparable to those in Phase 1.

Gross erosion rates were comparable to the values measured in Phase 1, in other words 1–2 $\times$ 10^{19} m^{-2}s^{-1} estimated both around the ISP and OSP during typical L-mode discharges (4 MW/400 kA) in the first high-fluence campaign in C7 [38]. The results indicate that increasing the pulse duration or fluence will not change the established picture on where the erosion-dominated regions are located poloidally: they just become more pronounced with increasing particle fluence and exhibit no synergistic effects that a largely increasing fluence might bring along.

The inner-outer asymmetry in W gross erosion was again visible. Depending on the scenario, up to a factor of ∼10 larger sputtering rates were measured on the inner than on the outer divertor, on the thick deposited layers, a few MBs away from the ISP [14]. This behaviour is illustrated in figure 9.

Additional data on the erosion behaviour was obtained from the analyses of so-called *fiducial markers* (square-like indents with an original width of 350 μm and depth of 50 μm) [25] on selected MBs after completing individual campaigns in Phase 2. The results, visualized in figure 8(*b*), demonstrate that the larger the accumulated fluence, the more the depth of the markers changes, and this trend is comparable both around the ISP and the OSP. On average a clear linear increase with the exposure time is observed from C6 to C11 and a distinct dependence on the toroidal position similarly to Phase 1. After >18 h of plasma time (from C6 to C11), the depth of the markers around the OSP at the ripple minimum had decreased by ∼12–27 μm while at the ISP minimum the decrease was ∼8 μm. Around the ISP maximum the decrease was somewhat larger, 7–20 μm, though some of the analysed MBs showed decreased crater depths, presumably due to the deposited material having accumulated at the bottom of the marker. Finally, the data from the OSP maximum indicated markers to have become >30 μm deeper but the reliability of the data is questionable due to cracks and other strong surface modifications on the MB surfaces. Conversion of changes in the depth of the markers to net erosion is challenging since deposition at the bottom of the markers has not been studied in detail, thus further post-exposure measurements and analyses are envisaged.

It is worth noting how differently the ripple minimum and maximum areas behaved during Phase 1 and Phase 2. In Phase 1, in particular the OSP minimum showed only low erosion compared to the OSP maximum while in Phase 2 no major differences were observed between the minimum and maximum ripple positions; one should, however, note the issues discussed above with the data from around the OSP maximum in Phase 2.

In the main chamber, the strongest sources were again located at the outer midplane, on the limiter structures surrounding the LH antennas, but their gross-erosion rates were at least a factor of two smaller than what was the case at the outer lower divertor.

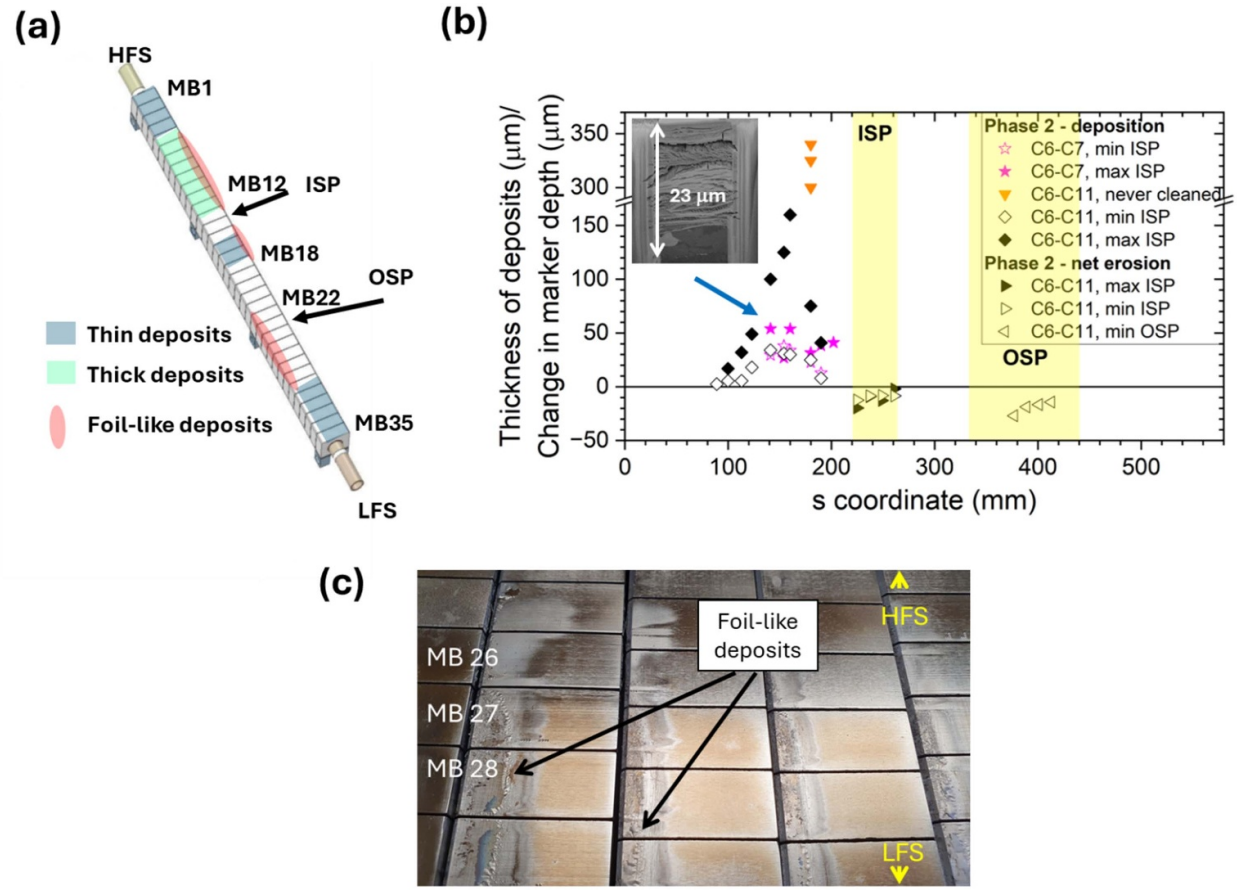


Figure 8. (*a*) Schematic illustration of the areas dominated by erosion (white) as well as thick and thin deposits (green and blue) and the so-called foil-like deposits (red) during Phase 2; (*b*) Evolution of the thickness of deposited layers and depths of the fiducial markers in Phase 2 together with an example cross-sectional SEM image of the structure of the thick co-deposited layers (here following exposures to C6–C7 campaigns) on WEST; (*c*) Photograph from one sector of the WEST divertor around the OSP region (MB26-MB28) after the high-fluence C7 campaign.

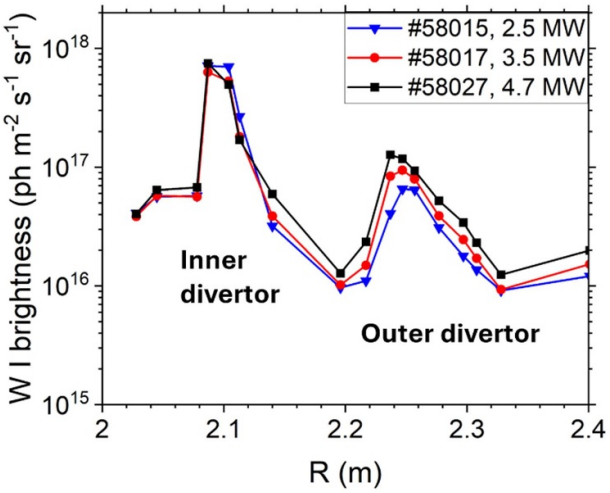


Figure 9. Divertor WI (400.9 nm) line emission extracted for L-mode plasma discharges with different heating powers as a function of the major radius R (see figure 2). The line-averaged densities of the relevant discharges were 3.3×10^{19} m^{-2} (#58015), 3.6×10^{19} m^{-2} (#58017), and 4.0×10^{19} m^{-2} (#58027).

4.2. Characteristics of deposited layers

The formation of the deposits is concentrated in the inner-divertor region also in Phase 2. Most detailed analyses have been performed after a high-fluence campaign in the end of C7 which consisted of repetitive long L-mode pulses (pulse length 60–70 s) in attached divertor conditions in D ($T_e \sim 25$ eV) [14]. The accumulated fluence of $\sim 5 \times 10^{26}$ m^{-2} was reached at the OSP region during some 3 h of plasma time while the maximum surface temperatures remained at modest values of ~400 °C, estimated from the peak heat load of 5 MWm^{-2} at the OSP [39]. A considerable number of unidentified flying objects (UFOs) hampered running the discharges towards the end of the high-fluence campaign phase as deposited layers were piling up [40]. The UFOs and the growth of the deposited layers were particularly noticeable during the last part of the campaign (about one third of it). As a result, intensive cleaning of the PFU surfaces was carried out, initially by applying double-sided tape on loosely bound layers. Whilst not producing dust inside the vessel, the method turned out to be inefficient in thorough cleaning of the PFUs and on average μm-sized layers remained on the surfaces [41]. More recently plasma and laser cleanings have been tested on the PFUs. The former, carried out during the C9 campaign by adjusting the ISP to coincide with the poloidal location of the thickest deposits, turned out not to be able to remove the deposits but instead generate a significant amount of impurities into the plasma [41]. However, the latter was demonstrated at laboratory scale and successfully applied after the C9 (two divertor sectors) and C11 (entire divertor) campaigns to remove all the deposits [9, 42].

Despite the higher particle fluence accumulated on the PFUs, the deposits were visually similar to those observed after the preceding campaigns. Figure 8(*b*) shows an SEM image (as an inset) of the structure of the thick deposits on an ITER-like PFU after the high-fluence campaign in C7 [43]. The deposited layers continued growing on average and could reach thicknesses of several hundreds of μm (>300 μm) in areas that were not cleaned in between campaigns as illustrated in figure 8(*b*). The ripple effect was considerable as well: Close to the ISP minimum, the layer thickness was ~25–40 μm while around the ISP maximum thicknesses of 100–140 μm were very consistently measured. The bevelling of the MBs in Phase 2 (no bevel in Phase 1, see figure 1) also played a role making the deposits thin toroidally on magnetically shadowed regions and increasing linearly towards the exposed areas. One could estimate that without cleaning such layers would result in considerable material inventories at the WEST divertor.

The estimated volume of the re-deposited layers within one ripple period and after 18 h of plasma, based on detailed microscopy investigations of tiles removed from different toroidal positions, is approximately 1.9 cm^3, thus the overall volume integrated across the entire circumference of the divertor (18 periods) is ~34 cm^3. The analysed deposits are not dense but contain porosities between the stacked layers (estimated to be in the order of 70%, see FIB image in figure 8(*b*)), which would lead to an estimate of ~24 cm^3 of 'dense' re-deposited material over the entire divertor. This material is made of 80%–100% of W, which would result in the deposited mass ranging between 370 g and 460 g [25]. The calculations were performed on PFUs cleaned during the shutdowns. However, as noted earlier, the volume of re-deposited layers is significantly higher when cleaning is not performed. The amount of material redeposited on the entire divertor could then double if no cleaning takes place.

All the deposited layers showed the same complex microstructure as previously reported in [8, 16, 19]: A mixture of low-*Z* and high-*Z* elements in a multilayer structure as well as signs of local melting and delamination. The deposits were relatively rich in W in the areas with the highest plasma flux, in the vicinity of the strike points where re-deposited tungsten plays a notable role, while further into the SOL, on the regions with thick deposits, the light elements O, B, C and N originating from other regions of the torus started to dominate the composition. The foil-like layers introduced in section 4.1, for their part, were different from the other deposits via showing a strong tendency to peel off when exposed to air [25, 43]. These films were only noticed on the magnetically shadowed areas of the MBs, toroidally towards their leading edges. The layers consisted almost exclusively of W and were strongly connected with the high-fluence operations. A photograph of the WEST OSP region after the C7 campaign, showing also the foil-like layers, is shown in figure 8(*c*).

The thick deposited layers as well as the notable erosion from specific wall components were considerable sources for dust in the reactor vessel in Phase 2 [44]. The analysed dust exhibited similar properties to the samples collected after Phase 1 in terms of their shape, size distribution and composition but now also a new class of dust particles could be found on the shadowed parts of the bevelled MBs. Most strikingly they were large in size (>100 μm), very likely originating from flaking of the thickest deposits as well as of the above-mentioned pure W layers. The large particles were present in notable quantities due to the many long plasma discharges carried out. In addition, dust nanoparticles could be observed throughout the divertor and prominently at varying depths within the layered co-deposits.

5. Modelling material migration on WEST

Tungsten erosion and migration in WEST plasmas has been extensively modelled primarily by SOLEDGE2D/3X [45, 46] and ERO2.0 [47] codes to further elucidate the contributions of the various W sources in the divertor and the main chamber regions [48, 49].

5.1. W gross and net erosion in Phase 1

In Phase 1, sputtering from the WEST PFUs has led to large W contents (n_W) in the plasmas and further to high values for the radiative fraction (f_{rad}), up to 50%, throughout the discharges almost independent of the applied heating power or

density. The simulations have shown that n_W is directly proportional to the power entering the SOL (P_{SOL}) and to the distance between the separatrix and the LH or ICRF antennas (Radial Outer Gap, briefly ROG) [47]. The lower divertor is the strongest W source during typical WEST plasma discharges, however, it is generally well screened over a wide range of background plasma parameters. Instead, the upper-divertor, baffle and other main-chamber regions provide a more direct access for the ejected W particles to penetrate into the core. This transport channel is the strongest at low densities due to the sources becoming more efficiently screened at denser plasmas [31]. Upon switching on RF sources, erosion from the respective antennas significantly increases. Modelling via the STRIPE simulation framework [50, 51] implies that RF sheath effects can increase erosion by more than an order of magnitude compared to the case where only thermal sheath conditions are taken into account.

In the simulations, oxygen is typically used as a proxy for the mixture of low-Z impurities in the SOL plasma. The most accurate agreement with the experimental data is obtained at low densities (within a factor of 1.5) by implying a low-Z background of a few at.% in the SOL while in the high-density regime gross erosion is systematically overestimated. This points towards obtaining an improved understanding of the complex interplay between the different sputtering agents and WEST wall structures at high densities, in particular at the divertor. On the other hand, sputtering from the main-chamber ICRF antennas is well captured by oxygen ions at high charge states as discussed in section 3.1 and at concentrations of ∼1 at.% [50].

The modelled net-erosion rates, for their part, are sensitive to the applied assumptions for the plasma and transport parameters but also on the material and surface characteristics like the morphology of the PFCs. Simulations generally underestimate net erosion, which is attributed to uncertainties in local re-deposition fractions, exceeding 95% in the simulations. Despite this, material migration pathways appear to be aligned with what has been established in other tokamaks including strong net W sources in the main chamber and transport into the HFS of the vessel to form thick deposits. The main open questions concerning the Phase 1 results are the experimentally observed strong inner–outer asymmetry in gross erosion (section 3.1) and the formation of thick deposits on the inner divertor surfaces (section 3.2.2). These can be attributed to the role of SOL flows and drifts similarly to what the corresponding studies on AUG have indicated [33] and what has been demonstrated by SOLPS-ITER simulations for seeded discharges at JET [52]. In addition, earlier modelling (see e.g. [53]) suggests that impurity (oxygen) concentrations can be much larger at the inner than at the outer side, which provides further evidence to enhanced erosion around the ISP. More work is also needed to properly account for the role of magnetic ripple in modulating erosion-deposition patterns and generally the 3D structure of erosion patterns on the PFCs [54]. Simulations have indicated that discrete local sources can dramatically increase W concentration in the main-chamber SOL and thereby penetration into the core.

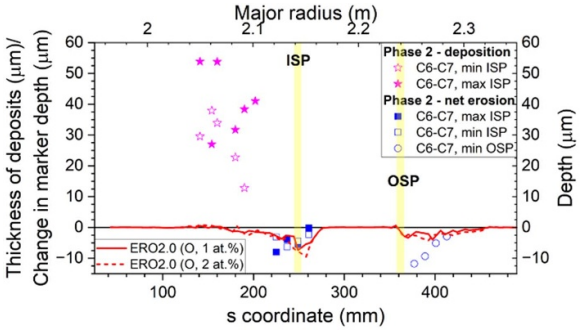


Figure 10. Simulated net erosion/deposition profile (ERO2.0) for the high-fluence campaign (right axis) for two different impurity (O as a proxy) concentrations together with the corresponding experimental data (left axis) measured either for the depth of the fiducial markers or the thickness of deposited layers after the C7 campaign. Negative values denote net erosion, positive values net deposition [38].

For the helium discharges during the C4 campaign, a multiscale simulation framework was adopted to reproduce the applied plasma conditions and make predictions for the W sputtering and He implantation profiles [55]. The main retention mechanism is considered to be implantation in W. According to data in figure 7(*b*), the contribution of co-deposition cannot be excluded but so far the analyses have only concentrated on the near-surface layer for the helium inventory. Again, the role of O is considerable: whilst it does not affect the implantation patterns, the overall He retention diminishes with increasing O content due to depletion of the near-surface layer by sputtering. All this highlights the key role of impurities in explaining not only erosion but also fuel retention characteristics and differences in these quantities for hydrogenic and helium plasmas.

5.2. Impact of high fluences on predicted erosion patterns in phase 2

The modelling efforts in Phase 2 have up to now concentrated on explaining the outcomes of the C7 high-fluence campaign at the divertor [38]. Much emphasis has been put on detailed determination of the fluxes by different impurity ions. Prompt re-deposition was taken into account in the simulations, that being >90% both on the inner and outer divertor, while other mechanisms such as drifts were excluded. Work to include drifts in the modelling workflow is ongoing [56]. The main light impurities in the plasma have been assessed to be B and C while O and N are also present but at smaller concentrations. As a result, the range of impurity levels applied in the simulations could be narrowed down to <5 at.% in terms of the effective O concentration. The simulated gross erosion is almost a factor of 10 higher both at the inner and the outer sides compared to the experimental observations, however, the predicted net erosion agrees with the experimental data, i.e. a couple of micrometres both at the ISP and OSP regions as figure 10 shows.

Instead, the main erosion peaks are predicted poloidally off from the highest flux regions by several centimetres and

the thick deposited layers next to the ISP region cannot be reproduced at all. Ongoing work aims at improving the agreement while laboratory investigations are being pursued to provide further insights into the physical mechanisms behind the formation of thick deposits. Here we would also like to highlight the role of missing drifts from the simulations as well as the lack of properly reconstructed impurity profiles that have been earlier observed to notably contribute to the observed erosion-deposition patterns at the divertor (see section 5.1) and finally the importance of correctly reproduced SOL flows. For the importance of the latter, fluid modelling has been able to predict the formation of thick re-deposits at the inner divertor, in the same poloidal region where they are experimentally observed [57]. Implementing SOL transport for the erosion workflow in ERO2.0 will be a topic of future studies.

6. Conclusions

We have reported here the collection of results obtained from extensive W erosion and migration investigations on WEST during its Phase 1 and Phase 2 plasma operations. The gross erosion of W is the strongest at the divertor region, however, due to its efficient screening the main-chamber sources may be much more prominent contributors to the transport of W into the core. Minimizing main-chamber erosion shall be achieved by carefully optimizing the applied discharge scenario including the RF sources which have been noticed to increase first-wall erosion by more than an order of magnitude. The large impurity content of the WEST SOL plasmas, including B, C, N, and O, leads to strong sputtering of W PFUs at the divertor region; for the first wall, modelling suggests highly-charged O ions to be responsible for W sputtering to a large extent.

The erosion-deposition patterns at the divertor generally agree with literature data from other tokamaks with the exceptions that net erosion is prominent both at the OSP and the ISP and that the deposits can reach values up to hundreds of micrometres if the PFCs are not regularly cleaned. In addition, the large net erosion reaching values of several tens of micrometres during $\sim$18 h of plasma time and continuously increasing with the accumulating fluence would be unacceptable in future devices.

Material migration characteristics, for their part, are in line with the established picture from AUG and JET. Erosion and deposition at the divertor appear to be local phenomena while the formation of the thickest deposits predominantly next to the ISP implies W transport in the SOL plasma from the LFS towards the HFS and strong main-chamber W sources to play a notable role in the overall material balance. However, there are still outstanding questions requiring further investigations via detailed modelling efforts. These include strong asymmetry in W sputtering at the divertor in favour of the inner side. Preliminary modelling efforts suggest drift flows together with the large impurity contents of the SOL plasmas on WEST to be the main candidates for the occurrence of the asymmetries.

The increase in pulse duration and plasma fluence from Phase 1 to Phase 2 does not result in radically different material-migration characteristics in the divertor region, as manifested by the relatively similar erosion and deposition behaviour poloidally in the two operational phases. Nevertheless, some qualitative changes start to emerge, including continuous growth of the deposits up to thicknesses of several hundreds of μm and a new class of foil-like layers forming on the tile surfaces. The formation of such deposits suggests a complex dependence on the exposure history of the PFCs, however, providing a full explanation to the origin, formation, and evolution of the extremely thick deposits with cumulated plasma exposure is a topic of future work.

The present work is intended as a synthesis of the erosion and migration observations accumulated during the first operational phases of WEST. While a number of recurring features have been identified, including strong ISP/OSP asymmetries, thick co-deposited layers, and significant tungsten redeposition, detailed quantitative explanations of these phenomena remain the subject of ongoing dedicated experimental and modelling activities

Acknowledgments

This work has been carried out within the framework of the EUROfusion Consortium, partially funded by the European Union via the Euratom Research and Training Programme (Grant Agreement No 101052200—EUROfusion). Views and opinions expressed are however those of the author(s) only and do not necessarily reflect those of the European Union or the European Commission. The European Union nor the European Commission can be held responsible for them. The work was partially supported by the Portuguese FCT foundation through project UID/50010/2025.

ORCID iDs

A. Hakola 0000-0003-1385-1296
M. Diez 0000-0002-8334-3521
N. Fedorczak 0000-0001-7123-7433
J. Gaspar 0000-0003-0104-1616
M. Balden 0000-0002-8755-9370
Y. Corre 0000-0002-6566-6116
S. Di Genova 0000-0003-4416-5600
A. Huart 0009-0003-8464-0629
C. Martin 0000-0002-4704-3273
I. Bogdanovic Radovic 0000-0002-4100-736X
E. Fortuna-Zalesna 0000-0002-1090-1641
E. Grigore 0000-0003-4470-3739
I. Jõgi 0000-0003-0007-8732
K. Krieger 0000-0003-0427-8184
A. Lagoyannis 0000-0003-1410-7944
J. Likonen 0000-0001-7676-7820
S. Markelj 0000-0002-6603-4006
R. Mateus 0000-0001-6733-6359
K. Mergia 0000-0002-2633-8750
P. Paris 0000-0002-0829-7510

P. Petersson 0000-0002-9812-9296
Z. Siketic 0000-0002-7358-8090
P. Tsavalas 0000-0001-5276-8108
T. Vuoriheimo 0000-0003-4266-9178
A. Widdowson 0000-0002-6805-8853

References

[1] Philipps V. 2011 *J. Nucl. Mater.* **415** S2–S9
[2] Hakola A. *et al* 2021 *Nucl. Fusion* **61** 116006
[3] Brezinsek S. *et al* 2019 *Nucl. Fusion* **59** 096035
[4] Ding R. *et al* 2015 *Nucl. Fusion* **55** 023013
[5] Bucalossi J. *et al* 2022 *Nucl. Fusion* **62** 042007
[6] Bucalossi J. *et al* 2024 *Nucl. Fusion* **64** 112022
[7] Diez M. *et al* 2023 *Nucl. Mater. Energy* **34** 101399
[8] Balden M. *et al* 2021 *Phys. Scr.* **96** 124020
[9] Bucalossi J. *et al* 2026 *Nucl. Fusion* **66** 116013
[10] Loarte A. *et al* 2025 *Plasma Phys. Control. Fusion* **67** 065023
[11] Krieger K. *et al* 2025 *Nucl. Fusion* **65** 043001
[12] Dumont R. *et al* 2025 WEST long-pulse achievements in support of next-step fusion devices *30th IAEA Fusion Energy Conf. Proc. Int. Conf.* (*Chengdu, China*)
[13] Tsitrone E. *et al* 2022 *Nucl. Fusion* **62** 076028
[14] Fedorczak N. *et al* 2024 *Nucl. Mater. Energy* **41** 101758
[15] Gaspar J. *et al* 2026 Overview of plasma wall interactions in the new high particle fluence campaign of WEST operated with cold divertor plasma conditions *27th Int. Conf. on Plasma-Surface Interactions in Controlled Fusion Devices Proc. Int. Conf.* (*Regensburg, Germany*)
[16] Balden M., Diez M., Hakola A., Mayer M. and Tsitrone E. 2026 *Nucl. Mater. Energy* **46** 102081
[17] Meyer O. *et al* 2016 *Rec. Sci. Instrum.* **87** 11E309
[18] Van Rooij G.J. *et al* 2020 *Phys. Scr.* **T171** 014060
[19] Martin C., Diez M., Campos A., Cabié M., Giacometti G., Balden M., Gallo A., Pegourié B., Bernard E. and Tsitrone E. 2021 *Phys. Scr.* **96** 124035
[20] Jõgi I., Paris P., Bernard E., Diez M., Tsitrone E., Hakola A., Likonen J., Vuoriheimo T. and Grigore E. 2023 *J. Nucl. Eng.* **4** 96–110
[21] Jõgi I., Paris P., Muru M.M., Diez M., Tsitrone E., Likonen J., Hakola A. and Grigore E. 2025 *Nucl. Mater. Energy* **45** 102004
[22] Hakola A. *et al* 2025 *Nucl. Mater. Energy* **45** 101998
[23] Mateus R., Catarino N., Alves E., Diez M., Bernard E., Tsitrone E., Balden M., Mayer M., Likonen J. and Hakola A. 2026 *Nucl. Mater. Energy* **46** 102050
[24] Tsavalas P. *et al* 2026 *Nucl. Fusion* **66** 036046
[25] Diez M. *et al* 2025 Overview of the results achieved from the characterization program of the WEST plasma facing components (2018–2024) *20th Int. Conf. on Plasma-Facing Materials and Components for Fusion Applications* (*Ljubljana, Slovenia*)
[26] Diez M. *et al* 2026 *Nucl. Mater. Energy* **47** 102135
[27] Gaspar J. *et al* 2022 *Nucl. Fusion* **62** 096023
[28] Klepper C.C. *et al* 2022 *Plasma Phys. Control. Fusion* **64** 104008
[29] Guillemaut C. *et al* 2025 *Nucl. Fusion* **65** 036007
[30] Grosjean A., Donovan D.C., Johnson C.A., Gunn J.P., Guillemaut C., Fedorczak N., Klepper C.C. and Unterberg E.A. 2023 *Nucl. Mater. Energy* **35** 101385
[31] Di Genova S. *et al* 2021 *Nucl. Fusion* **61** 106019
[32] Pitts R.A. *et al* 2005 *J. Nucl. Mater.* **337–9** 146–53
[33] Hakola A., Keitaanranta A., Kumpulainen H., Lahtinen A., Likonen J., Balden M., Cavedon M., Krieger K., Airila M. and Groth M. 2020 *Nucl. Mater. Energy* **25** 100863
[34] Fortuna-Zalesna E. *et al* 2016 *Nucl. Mater. Energy* **9** 128–31
[35] Grosjean A. *et al* 2020 *Nucl. Fusion* **60** 106020
[36] Marin A., Saefan A., Unterberg E., Parish C.M., Bernard E., Diez M., Tsitrone E. and Wang X. 2025 *J. Nucl. Mater.* **604** 155525
[37] Arnas C. *et al* 2023 *Nucl. Mater. Energy* **36** 101471
[38] Huart A. *et al* 2025 *Nucl. Mater. Energy* **45** 102017
[39] Corre Y. *et al* 2023 *Nucl. Mater. Energy* **37** 101546
[40] Gaspar J. *et al* 2024 *Nucl. Mater. Energy* **41** 101745
[41] Gerardin J. *et al* 2024 *Nucl. Mater. Energy* **41** 101783
[42] Firdaouss M. *et al* 2025 *Ex-situ* and *in-situ* laser cleaning of divertor tungsten surface for tokamak *22nd Int. Conf. on Fusion Reactor Materials Proc. Int. Conf.* (*Shizuoka, Japan*)
[43] Martin C., Diez M., Bernard E., Cabié M., Campos A., Pardanaud C., Giacometti G., Gallo A., Gaspar J. and Corre Y. 2024 *Nucl. Mater. Energy* **41** 101764
[44] Arnas C., Campos A., Diez M., Bernard E., Brun C., Martin C., Gensdarmes F., Peillon S. and Tsitrone E. 2025 *Nucl. Mater. Energy* **42** 101848
[45] Bufferand H. *et al* 2015 *Nucl. Fusion* **55** 053025
[46] Bufferand H. *et al* 2021 *Nucl. Fusion* **61** 116052
[47] Romazanov J. *et al* 2019 *Nucl. Mater. Energy* **18** 331
[48] Di Genova S. *et al* 2024 *Nucl. Fusion* **64** 126049
[49] Gallo A. *et al* 2020 *Phys. Scr.* **T171** 014013
[50] Kumar A. *et al* 2025 *Nucl. Fusion* **65** 076039
[51] Kumar A. *et al* 2026 *EPJ Web Conf.* **346** 01004
[52] Kaveeva E., Rozhansky V., Veselova I., Senichenkov I., Giroud C., Pitts R.A., Wiesen S. and Voskoboynikov S. 2021 *Nucl. Mater. Energy* **28** 101030
[53] Gallo A. *et al* 2020 *Nucl. Fusion* **60** 126048
[54] Di Genova S. *et al* 2023 *Nucl. Mater. Energy* **34** 101340
[55] Lasa A. *et al* 2024 *Nucl. Fusion* **64** 106012
[56] Huart A. *et al* 2026 Erosion and deposition patterns on ITER-grade actively-cooled divertor in WEST high-fluence campaign: analysis and comparison with SOLEDGE3X and ERO2.0 modeling results *27th Int. Conf. on Plasma-Surface Interactions in Controlled Fusion Devices* (*Regensburg, Germany*)
[57] Varadarajan N. *et al* 2026 Integrated core-edge modelling of tungsten using SOLEDGE-3X and application to WEST experiment *27th Int. Conf. on Plasma-Surface Interactions in Controlled Fusion Devices* (*Regensburg, Germany*)